Rev. Roum. Sci. Techn.– Électrotechn. et Énerg.
Vol. **71**, *3*, pp. 355–360, Bucarest, 2026

AN ENHANCED STRAY FLUX APPROACH FOR ROTOR BAR FAULT DETECTION IN INDUCTION MACHINES

ASSAM ZORIG[1], BADREDDINE BABES[2], NOUREDDINE HAMOUDA[2], KHALED BELHOUCHET[1], SHERIF S.M. GHONEIM[3]

Keywords: Broken bars; Diagnostic; Finite element analysis; Induction motors; Modeling; Monitoring; Signal processing.

This paper presents an enhanced method for detecting broken rotor bar (BRB) faults in squirrel-cage induction motors (SCIMs), with a focus on low- and no-load conditions. The approach relies on harmonic analysis of stray magnetic flux and is benchmarked against conventional Motor Current Signature Analysis (MCSA). Fault scenarios, including single and multiple broken bars in adjacent and non-adjacent configurations, are investigated using finite element simulations of a 2.2 kW motor. Results show that stray flux indicators provide higher sensitivity and accuracy than stator current–based methods. Experimental validation under varying load conditions (slip 0.049–0.092) confirms the effectiveness of the proposed approach, particularly under no-load operation. These findings highlight its suitability for real-time condition monitoring and predictive maintenance of SCIMs.

1. INTRODUCTION

Squirrel-cage induction motors (SCIMs) are widely used in industrial and domestic applications. However, faults in these motors can lead to severe operational and economic losses, making early detection and accurate diagnosis essential [1,2]. SCIM faults are generally classified as electrical or mechanical, and may occur in the stator or rotor. Among them, Broken Rotor Bar (BRB) faults are particularly critical, as they degrade motor performance, reduce starting torque, and introduce thermal and mechanical stresses that accelerate overall system deterioration.

Over the past decades, various diagnostic techniques have been developed for BRB detection [3]. Among them, Motor Current Signature Analysis (MCSA) is widely used due to its simplicity and effectiveness in frequency-domain analysis [4]. Nevertheless, MCSA suffers from limitations such as false positives and false negatives under certain operating conditions, which has motivated the exploration of alternative approaches [5]. These include vibration analysis [6], temperature monitoring [7], Park's vector methods [8], and artificial intelligence–based techniques [9], most of which rely on prior knowledge of healthy motor behavior.

To overcome these limitations, stray magnetic flux analysis (SMFA) has emerged as a promising non-invasive diagnostic method [10]. Faults in SCIMs generate characteristic signatures in the stray flux spectrum, which can be captured using external sensors and analyzed to identify rotor defects. Previous studies have shown that both supply-frequency sidebands and low-frequency harmonics are sensitive indicators of BRB faults. While transient (startup) analysis enhances fault detectability, it is not suitable for continuously operating motors, making steady-state approaches more practical. Recent research highlights the effectiveness of mechanical harmonics in stray flux signals for detecting BRB faults with high sensitivity. However, most existing methods focus on limited spectral components, restricting the full utilization of available diagnostic information, especially in low-slip machines.

In this context, the present work proposes a novel and robust methodology for detecting BRB faults, including non-adjacent defects, using mechanical harmonics of stray magnetic flux under steady-state operation. The approach employs a simple external sensor and demonstrates high sensitivity under varying load conditions, enabling reliable online monitoring and early fault detection to prevent downtime and maintain SCIM performance.

2. MODELING OF BRBS BASED ON FINITE ELEMENT ANALYSIS (FEA)

In this section, an SCIM is modeled and simulated using FLUX-2D to analyze its behavior under BRB fault conditions. Accurate Finite Element Analysis (FEA) requires proper definition of geometry, material properties, meshing, and boundary conditions. To ensure a balance between computational efficiency and model accuracy, simplified geometry and appropriate material assumptions are adopted [11]. The main electrical and geometric parameters of the stator and rotor are summarized in Table 1. The stray magnetic flux is measured using an external search-coil sensor placed near the machine [12].

Table 1

Electrical and geometric parameters of the stator and rotor

Specification	Characteristics	Value	Unit
Machine	Nominal power rating	2.2	kW
	Nominal operating voltage	400	V
	Nominal current	4.8	A
	Rated rotational speed	1418	rpm
	Stator phase number	3	-
	Pole number	4	-
	Supply frequency	50	Hz
Stator	Connection configuration	Star	-
	Slot number	36	-
	Inner diameter	99	mm
	Outer diameter	173	mm
Rotor	Airgap length	0.33	mm
	Total number of rotor bars	48	-
	Inner diameter	34	mm
	Outer diameter	98.1	mm

The Flux-2D solves the electromagnetic field problem by implementing the following equation:

$$\sigma_e \frac{\partial \mathbf{A}}{\partial t} + \mathrm{curl}\left(\frac{1}{\mu}\mathrm{curl}\mathbf{A}\right) = \mathbf{J} + \mathrm{curl}\mathbf{H}. \quad (1)$$

Here, **H** [A/m] represents the magnetic field strength, **A** [Wb/m] represents the magnetic vector potential, **J** [A/m^2] denotes the current density, σ [S/m] is the electrical conductivity, and μ [H/m] refers to the magnetic permeability.

All FEA simulations are performed by coupling the magnetic field equations with an external electric circuit supplied by a voltage source to ensure a realistic model. Figure 1 illustrates the motor geometry and the associated electrical circuit modeled in Flux-2D. A search-coil (stray flux) sensor with 1200 turns is placed 110 mm from the

[1]Electrical Engineering Laboratory (LGE), Faculty of Electrical Engineering, University of M'Sila, 28000 M'Sila, Algeria.
[2]Research Center in Industrial Technologies (CRTI), P.O. Box 64, Chéraga 16014, Algiers, Algeria.
[3]Department of Electrical Engineering, College of Engineering, Taif University, Taif 21944, Saudi Arabia.
…E-mails: assam.zorig@univ-msila.dz, khaled.belhouchet@univ-msila.dz, b.babess@crti.dz, n.hamouda@crti.dz, s.ghoneim@tu.edu.sa

DOI: 10.59277/RRST-EE.2026.3.3

SCIM center and oriented perpendicular to the shaft to measure the voltage induced by the radial component of the stray magnetic flux.

Four operating conditions are considered: a healthy machine and three BRB fault cases (one broken bar, two adjacent broken bars, and two non-adjacent broken bars). In the FEM model, faults are simulated by increasing the resistance of the affected bar by a factor of 100, representing a near-open-circuit condition [4].

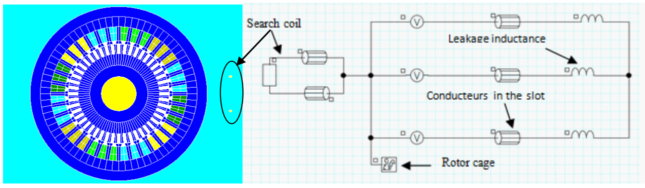

(a) (b)

Fig. 1 – Finite element–based magnetic field modeling (a) detailed geometric representation of the SCIM (b) coupled electrical circuit used for electromagnetic simulation in Flux-2D.

3. METHODOLOGY

This study proposes a methodology based on the analysis of radial stray flux signals to enhance the detection of BRB faults in SCIMs. The proposed approach demonstrates higher sensitivity compared to conventional MCSA techniques. The external magnetic flux density is measured under both no-load and load conditions using a custom-built sensor. Fig. 2 shows the distribution of radial stray flux lines and the positioning of the coil-based sensor, which captures the flux through the induced voltage proportional to its rate of change. In this study, the signal analysis focuses on tracking variations in the amplitudes of mechanical harmonic components in the radial stray flux associated with rotor faults. The presence of BRB faults is reflected in the Fourier spectrum as characteristic harmonic components (f_b), whose frequencies can be determined using:

$$f_b = kf_r \pm s, \tag{2}$$

where k is a positive integer, f_r represents the rotor mechanical frequency, defined as $f_r = (1–s)f_s/p$, and p denotes the SCIM's pole pair count.

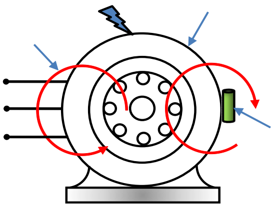

Fig. 2 –Conceptual radial stray flux path and associated sensor placement for flux measurement.

4. FEA SIMULATIONS

Figure 3 shows the effect of BRB faults on the spatial magnetic field distribution under nominal load conditions. Each fault induces a magnetic asymmetry whose magnitude depends on its location and severity. This asymmetry is mainly caused by eddy currents in the rotor slots and slip variations, along with the influence of harmonic currents and local magnetic saturation. For all fault cases, the maximum magnetic flux density is higher than in the healthy motor. This increase, combined with local saturation effects, explains the rise in stator current under nominal load despite the higher rotor resistance introduced by the broken bars.

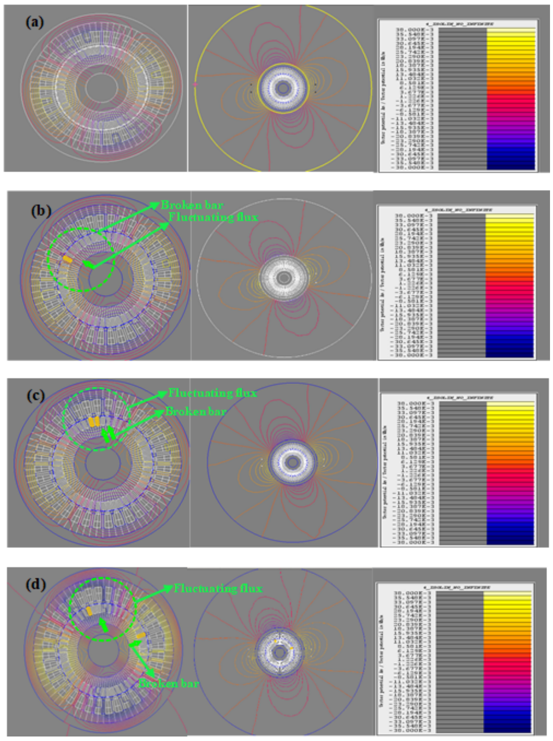

Fig. 3 –A comparative analysis of magnetic fields for different rotor faults, showing internal flux distribution (left) and external field lines (right): (a) healthy operation; (b) one broken bar; (c) two adjacent broken bars; (d) two non-adjacent broken bars.

The FEA simulation is conducted over a 1.5 s steady-state interval, including speed ripple effects. The stray magnetic flux and stator current signals are sampled at 10 kHz. Figure 4 compares the time-domain responses of the stator current and stray flux under healthy and faulty conditions. As shown in Fig. 4, the BRB faults have a weak and barely distinguishable effect on the stator current, with only slight amplitude modulation. In contrast, the induced voltage from the stray flux sensor provides a clearer indication of motor condition. Under faulty operation, the signal exhibits noticeable variations compared to the healthy case (Fig. 4), which become more pronounced as the number of broken bars increases. Figure 5 shows the rotor speed and electromagnetic torque under full-load conditions. The results highlight the impact of BRB faults, which introduce distortions that lead to noticeable fluctuations in both torque and speed. Figure 5 (zoomed between 0.5 s and 1.5 s) reveals low-frequency speed oscillations with amplitudes ranging from 4 to 6 rpm. These fluctuations reduce the average rotor speed, resulting in increased slip to maintain the load torque. Consequently, a corresponding reduction in electromagnetic torque is observed, as illustrated in Fig. 5.

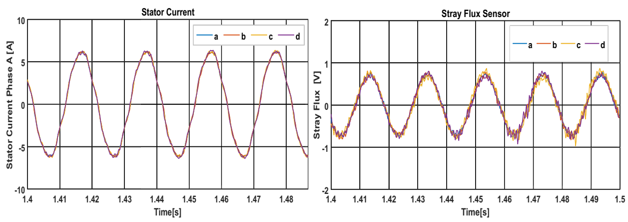

Fig. 4 –Stator current and stray flux signals under full-load operation: (a) healthy motor; (b) motor with a single breakage rotor bar; (c) motor with two adjacent breakage bars; (d) motor having two non-adjacent breakage bars.

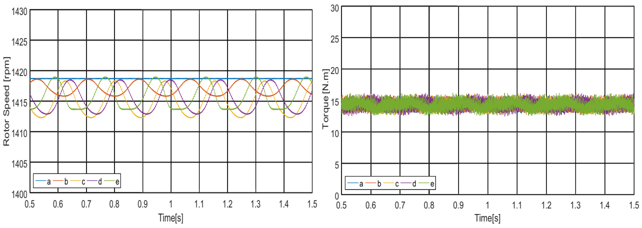

Fig. 5 –Rotor speed and electromagnetic torque signals at full load condition: (a) healthy motor; (b) motor with a single breakage rotor bar; (c) motor with two adjacent breakage bars; (d) motor having two non-adjacent breakage bars.

5. MCSA RESULTS

This section analyzes stator current signatures using motor current signature analysis (MCSA) under varying load conditions. The frequency spectra for full-load, half-load, and no-load operations are shown in Fig. 6. As expected, characteristic fault-related harmonics such as sidebands at $k f_s \pm 2\, sf_s$ and components around odd multiples of the supply frequency ($3f_s$, $5f_s$, and $7f_s$) are clearly visible under full and half-load conditions. However, these components become nearly undetectable under no-load operation (Fig. 6). This limitation arises because MCSA relies on slip-dependent frequency modulation; as slip approaches zero, fault-related harmonics significantly attenuate, reducing the signal-to-noise ratio. Consequently, reliable fault detection becomes challenging under light-load conditions, increasing the risk of false indications, especially when the number and location of broken rotor bars are unknown.

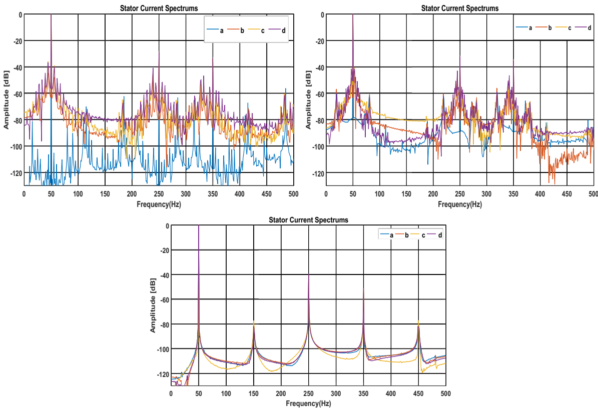

Fig. 6 –Stator current spectral analysis at full-load, half-load, and at non-load conditions: (a) Healthy motor; (b) motor with a single breakage rotor bar; (c) motor with two adjacent breakage bars; (d) motor having two non-adjacent breakage bars.

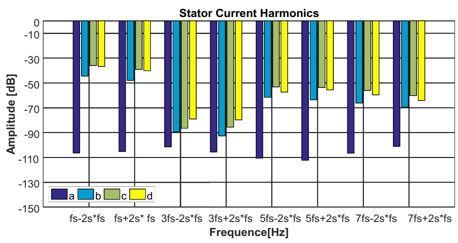

Fig. 7 –Harmonic amplitudes of stator current at $k f_s$+$2sf_s$ under full-load operation: (a) healthy motor; (b) motor with a single breakage rotor bar; (c) motor with two adjacent breakage bars; (d) motor having two non-adjacent breakage bars.

Figure 7 presents the amplitude of fault-related harmonics for different rotor conditions. Compared to a healthy rotor, the amplitude increases by more than 60 dB in the presence of a single broken bar.

For two adjacent broken bars, an additional increase of about 10 dB is observed. In contrast, the amplitude for two non-adjacent broken bars is approximately 3 dB lower than that of adjacent faults, although still significantly higher than the healthy case. This trend highlights the reduced sensitivity of MCSA in detecting non-adjacent BRBs, potentially leading to false-negative diagnoses as amplitudes approach typical detection thresholds.

6. SFSA RESULTS

This section analyzes the harmonic content of the radial stray magnetic flux for rotor fault detection. Figure 8 shows the frequency spectra for healthy and faulty motors, including one broken bar, two adjacent, and two non-adjacent broken bars. Unlike stator current, the stray flux exhibits a higher density of harmonics, particularly at mechanical frequencies such as $kf_r$$-2sf_s$. For instance, the $f_r$$-2sf_s$ component increases from –112 dB in the healthy motor to -46.7 dB, -38.2 dB, and -42.1 dB for one broken bar, two adjacent bars, and two non-adjacent bars, respectively, under full load. Pronounced sidebands at $kf_r \pm 2sf_s$ are consistently observed in all fault cases and increase with mechanical load. At low slip, these sidebands are often masked by spectral leakage from dominant harmonics, which limits MCSA effectiveness in low-slip motors. The results confirm that stray flux analysis reliably detects rotor defects even when MCSA produces false positives or negatives.

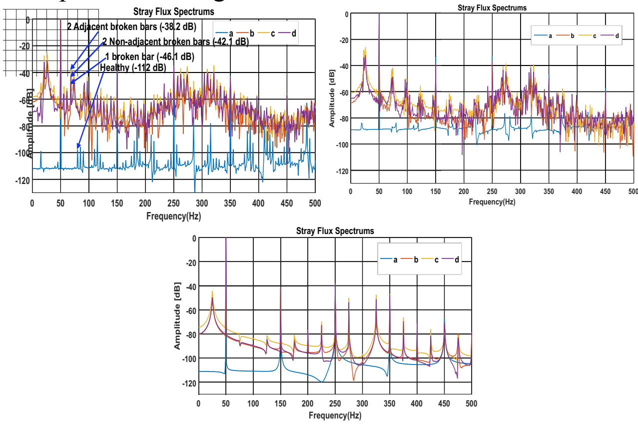

Fig. 8 –Stray magnetic flux spectra under full-load, half-load, and at non-load conditions: (a) healthy motor; (b) motor with a single breakage rotor bar; (c) motor with two adjacent breakage bars; (d) motor having two non-adjacent breakage bars.

Figure 9 shows the kfs+$2sf_s$ harmonic in the stray magnetic flux under full-load operation for healthy and faulty motors.

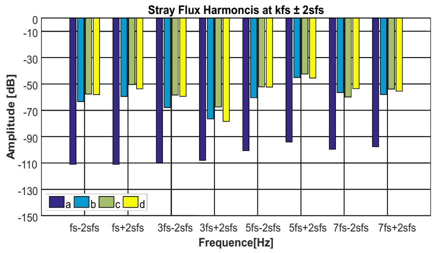

Fig. 9 –Harmonic amplitude of stray magnetic flux at the frequency component kf_s±$2sf_s$ under full-load operation: (a) Healthy motor; (b) motor with a single breakage rotor bar; (c) motor with two adjacent breakage bars; (d) motor having two non-adjacent breakage bars.

The amplitude increases significantly in the presence of BRB faults: a single broken bar raises it by ~65 dB, two adjacent bars increase it by an additional 5 dB, while two non-adjacent bars exhibit an amplitude ~2 dB lower than the adjacent case, yet still well above the healthy motor level.

Figure 10 shows the mechanical harmonic components at $kf_r \pm sf_s$ in the stray flux spectrum. In the healthy motor, these components are very weak (approximately –115 dB). A single broken bar increases the amplitude to approximately –35 dB (≈80 dB gain), while two adjacent bars further raise it to approximately –27 dB (additional ~8 dB). Two non-adjacent bars yield slightly lower amplitudes (approximately –32 dB), still more than 80 dB above the healthy motor. Across all broken-bar scenarios, the $kf_r \pm sf_s$ components increase by over 25 dB regardless of load or fault location. These results confirm a clear monotonic relationship between fault severity and harmonic amplitude, highlighting that $kf_r \pm sf_s$ components are robust and quantifiable indicators for BRB detection. Overall, stray flux analysis effectively reveals mechanical-related harmonics that are weak or masked in stator current spectra, providing a reliable method for rotor fault diagnosis under full-load conditions.

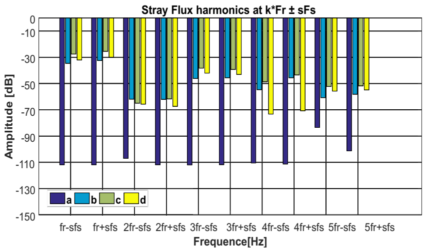

Fig. 10 –Stray flux harmonics amplitude at rank of $kf_r \pm sf_s$ at full load condition (a) Healthy motor (b) motor with a single breakage rotor bar (c) motor with two adjacent breakage bars (d) motor having two non-adjacent breakage bars.

Table 2 summarizes the amplitudes of the $f_r \pm 2sf_s$ harmonics in the stray flux under full-load conditions, showing clear sensitivity to BRB faults. For a single broken bar at rated load, the $f_r - 2sf_s$ and $f_r + 2sf_s$ components increase by approximately 66 dB and 34 dB, respectively. Across different loads and fault severities, the $kf_r \pm sf_s$ and $f_r \pm 2sf_s$ harmonics consistently provide reliable indicators for detecting broken rotor bars.

Table 2

Amplitudes of the harmonics at rank $f_r \pm 2sf_s$ of the stray flux at full load

Motors cases	f_r-$2sf_s$	f_r+$2sf_s$
Healthy machine	–112 dB	–97 dB
One breakage bar	–46.1 dB	–63.1 dB
Two adjacent breakage bars	–38.2 dB	–63.4 dB
Two non-adjacent breakage bars	–42.1 dB	–65.4 dB

The comparative results show that the proposed RSFA method outperforms both MCSA and vibration-based techniques across all evaluated criteria. This superiority arises from three key advantages: (*i*) a richer physical signal representation, (*ii*) robust diagnostic features under varying load and speed, and (*iii*) high sensitivity to incipient rotor faults. RSFA reliably extracts weak fault signatures in noisy conditions by tracking fundamental components and associated sidebands while suppressing baseline noise. In contrast, MCSA is limited by slip dependence and operating conditions, causing spectral overlap and fault masking, especially at low load. Vibration-based methods rely on torque ripple and mechanical transmission, reducing sensitivity to early-stage BRB faults under light-load or near-synchronous conditions. RSFA, however, maintains robust performance even at no-load or low-speed, making its diagnostic indicators largely independent of operating point, enabling reliable early fault detection and minimizing false negatives compared to conventional methods.

7. **EXPERIMENTAL VALIDATION**

To validate the proposed stray flux-based detection method, an experimental test bench was set up at the Modeling, Information, and Systems Laboratory of the University of Picardy Jules Verne. Figure 11 illustrates the experimental diagnostic procedure applied to the SCIM. The experiments aimed to replicate real-world operating conditions, including noise, harmonics, and external disturbances. A three-phase SCIM (Table 3) was connected to a variable mechanical load (Fig. 11a), with currents measured via sensors (Fig. 11b). Two magnetic flux sensors were used to capture the stray flux EMF: a commercial DRV425 fluxgate sensor (Fig. 11c) and a lab-fabricated search coil (~50 mm diameter, 1100 turns, Fig. 11d) mounted on the motor frame to measure both radial and axial components while avoiding shaft installation difficulties. Measurements were taken under steady-state conditions for three scenarios: healthy motor at rated load, no load, and half load. Signals were acquired using a dSPACE ds1104 board at 25 kHz sampling over 0.2 s per point and processed in MATLAB to analyze harmonic evolution.

Table 3

Motor parameters for experimental laboratory.

Parameter	Value / Unit
Coupling type	Star
Nominal power	3 kW
Nominal voltage	400 V
Nominal current	6.4 A
rotational speed	1340 tr/min
Supply frequency	50 Hz
Total number of pole pairs	2

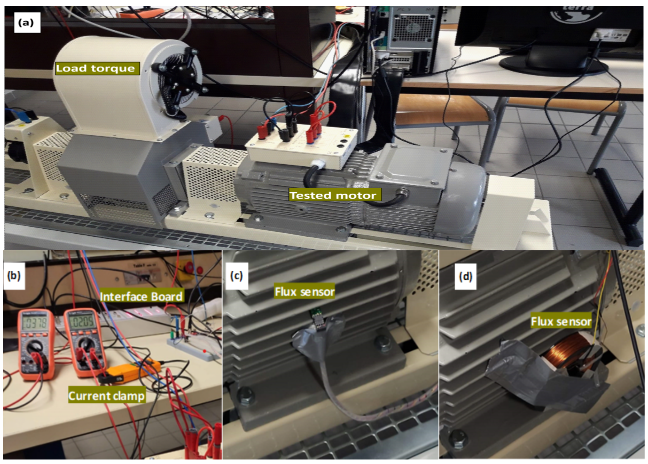

Fig. 11 –Experimental testbed for data acquisition from the healthy SCIM: (a) motor-load test bench; (b) current clamp; (c) placement of the DRV425 fluxgate sensor, and (d) placement of the search-coil sensor.

7.1 RESULT ANALYSIS OF THE HEALTHY MOTOR UNDER FULL-LOAD CONDITION (s = 0.092)

The stator current spectrum in Fig. 12.a is dominated by the supply frequency, with remaining harmonics at low amplitudes and partially masked by noise, highlighting the limited sensitivity of current-based analysis to weak disturbances. In contrast, the stray flux spectra from the fluxgate and search-coil sensors (Figs. 12b and 12c) display richer harmonic content, with additional components at higher amplitudes, reflecting the localized sensitivity of stray flux to magnetic field variations in the air gap and rotor.

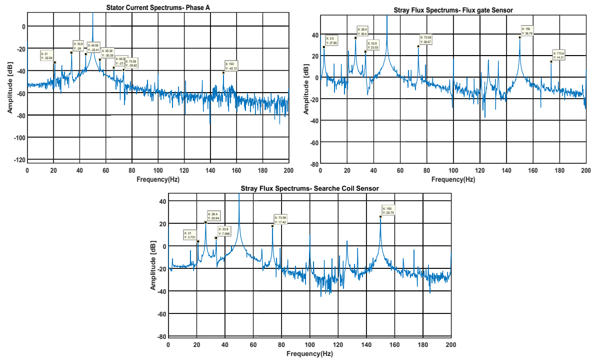

Fig. 12 –Spectral analysis under normal operating at full-load condition: (a) stator current spectrum of phase–A; (b) stray flux EMF spectrum measured using the fluxgate sensor, and (c) stray flux EMF spectrum measured using the search-coil sensor.

7.2 RESULT ANALYSIS OF THE HEALTHY MOTOR UNDER NO-LOAD CONDITION (s = 0.049)

The stator current spectrum is dominated by the fundamental supply frequency, with higher-order harmonics at low amplitudes near the noise floor (Fig. 13a). Similarly, the stray flux spectra from the fluxgate and search-coil sensors exhibit few low-amplitude components (Figs. 13b and 13c), as expected under no-load conditions with minimal rotor currents and air-gap distortions. Nevertheless, the stray flux signals show richer harmonic content than the stator current, reflecting greater sensitivity to local magnetic field variations.

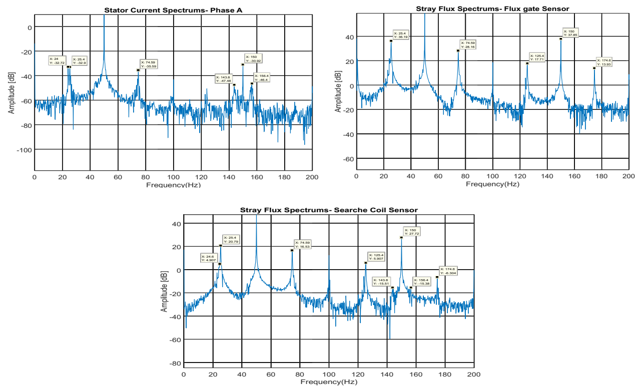

Fig. 13 –Spectral analysis under normal operating at no-load condition: (a) stator current spectrum of phase–A; (b) stray flux EMF spectrum measured using the fluxgate sensor, and (c) stray flux EMF spectrum measured using the search-coil sensor.

7.3 RESULT ANALYSIS OF THE HEALTHY MOTOR UNDER HALF-LOAD CONDITION (s = 0.066)

Compared to no-load, the stator current under half-load conditions remains dominated by the 50 Hz supply frequency, with slightly higher amplitude and higher-order harmonics below −50 dB, confirming healthy operation (Fig. 14a). In the stray flux spectra (Figs. 14b and 14c), additional harmonics are more pronounced in the 0–200 Hz range, particularly at 50 Hz and its multiples (100 Hz, 150 Hz), with amplitudes between -30 and -20 dB depending on the sensor. No fault-related sidebands are observed, indicating normal electromagnetic behavior under half-load.

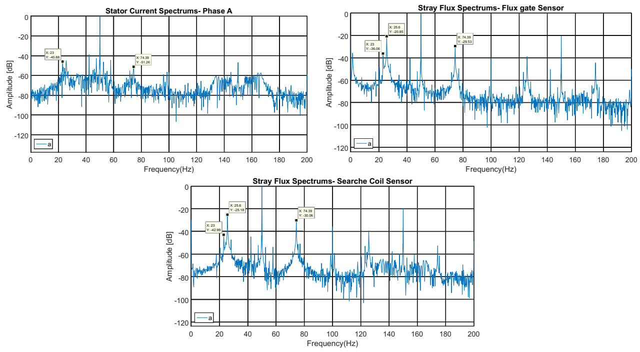

Fig. 14 –Spectral analysis under normal operating at half-load condition: (a) stator current spectrum of phase–A; (b) stray flux EMF spectrum measured using the fluxgate sensor, and (c) stray flux EMF spectrum measured using the search-coil sensor.

7.4 RESULT ANALYSIS OF A SINGLE BRB FAULT UNDER FULL-LOAD CONDITIONS (s = 0.092)

The experimental results presented in Fig. 15 demonstrate that, although the stator current analysis can detect the single BRB fault, the stray flux–based techniques, particularly using a search coil sensor, provide higher sensitivity and clearer fault identification under full-load conditions. Compared with stator current analysis (Fig.15a), the stray flux spectra obtained from both the search coil and flux gate sensors (Fig.15b and Fig. 15c) exhibit more pronounced sidebands around the $kf_r \pm 2sf_s$ frequency, indicating enhanced sensitivity to the presence of a single BRB fault.

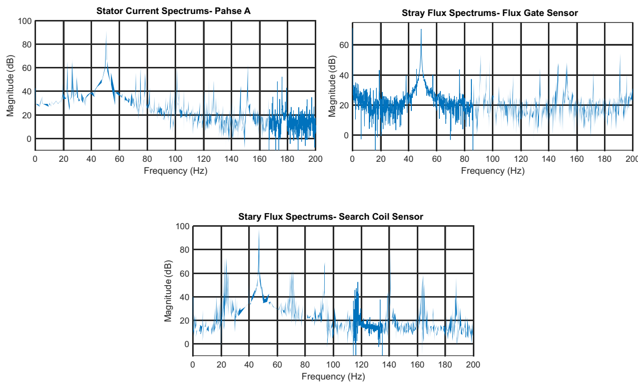

Fig. 15 –Spectral analysis under a single BRB fault at full-load condition: (a) stator current spectrum of phase–A; (b) stray flux EMF spectrum measured using the fluxgate sensor, and (c) stray flux EMF spectrum measured using the search-coil sensor.

7.5 RESULT ANALYSIS OF A SINGLE BRB FAULT UNDER NO-LOAD CONDITION (s = 0.049)

Under no-load operation with a single BRB fault, as shown in Fig. 16, the fault indicators remain evident using stray flux techniques (Fig. 16b and Fig. 16c) despite the reduced electromagnetic coupling. The stray magnetic flux spectrum exhibits distinct sideband components around the $kf_r \pm 2sf_s$ frequency, consistent with the characteristic effects of a single BRB fault. These components confirm the theoretical FEA model and highlight the high sensitivity of stray flux-based methods. In contrast, stator current analysis (Fig.16.a) shows weaker and less pronounced fault indicators under similar no-load operating conditions.

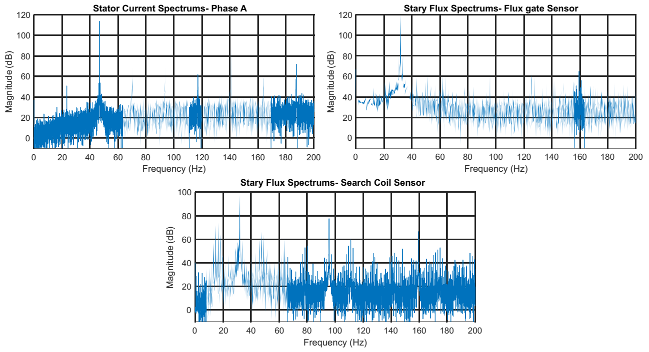

Fig. 16 –Spectral analysis under a single BRB fault at no-load condition: (a) stator current spectrum of phase–A; (b) stray flux EMF spectrum measured using the fluxgate sensor, and (c) stray flux EMF spectrum measured using the search-coil sensor.

7.6 RESULT ANALYSIS OF A SINGLE BRB FAULT UNDER HALF-LOAD CONDITION (s = 0.066)

Under half-load operation, the single BRB fault signal is more pronounced than under no-load operation, as shown in Fig. 17. The stator current spectrum (see Fig. 17a) exhibits more pronounced sidebands, despite its moderate amplitude and noise sensitivity. On the other hand, the stray flux spectra from the flux gate sensor and search coil (see Fig. 17b and Fig. 1.7c) show a stronger and more pronounced sideband. In general, increasing the load increases fault detection sensitivity, and stray-flux techniques offer higher sensitivity than stator-current analysis.

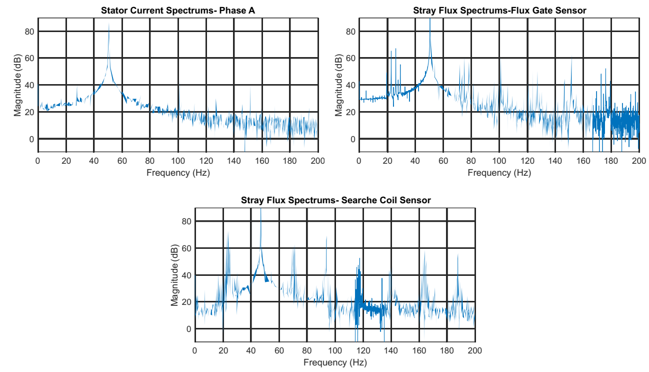

Fig. 16 –Spectral analysis under normal operating at half-load condition: (a) stator current spectrum of phase–A; (b) stray flux EMF spectrum measured using the fluxgate sensor, and (c) stray flux EMF spectrum measured using the search-coil sensor.

9. **CONCLUSIONS**

This study proposes a reliable stray flux–based method for detecting broken rotor bar (BRB) faults in SCIMs. A finite-element SCIM model was developed and validated as a virtual test bench to analyze machine behavior under healthy and faulty conditions. Diagnostic analysis focused on stray flux components at $kf_r \pm sf_s$ and $kf_r \pm 2sf_s$, including the first, third, fifth, and seventh harmonic sidebands, as well as mixed-frequency components $f_s + f_r \pm 2sf_s$. These components exhibited superior sensitivity compared to conventional MCSA, particularly under low-slip or challenging operating conditions. The identified features remained robust across variations in fault location and load, enabling consistent and reliable detection. Supported by low-cost external flux sensors, the approach offers a practical solution for real-time condition monitoring and predictive maintenance. Experimental validation on a healthy SCIM under different loads confirmed the method's effectiveness, especially under no-load conditions. Future work will investigate half-broken rotor bar scenarios to further evaluate the sensitivity, robustness, and detection limits of the proposed technique.

ACKNOWLEDGMENTS:

The authors would like to acknowledge the Deanship of Graduate Studies and Scientific Research at Taif University for funding this work.

CREDIT AUTHORSHIP CONTRIBUTION STATEMENT

ASSAM ZORIG: conceptualization, methodology, writing of the original draft.
BADREDDINE BABES: investigation, writing, review & editing.
NOUREDDINE HAMOUDA: supervision, resources, results curation.
KHALED BELHOUCHET: visualization, writing, review & editing.
SHERIF S. M. GHONEIM: supervision, resources, results curation.

Received on 23 March 2026

REFERENCES

1. A.G. Yetgin, M.M. Tezcan, *Effect of the lambda parameter on three-phase induction motor design by analytical and magnetic methods*, Rev. Roum. Sci. Techn. – Électrotechn. et Énerg., **70**, *4*, pp. 435–440 (2025).
2. E.-G. Boudissa, M. Bounekhla, F. Habbi, *Enhanced spiral dynamic algorithm with application to induction motor parameters identification*, Rev. Roum. Sci. Techn. – Électrotechn. et Énerg., **70**, *4*, pp. 441–446 (2025).
3. J. Li, C. Zheng, Z. Wu, H. Chen, X.-B. Wang, Z.-X. Yang, *Review of fault diagnosis for rotating machinery: Prior knowledge integration in data-driven methods benefits model interpretability and generalizability*, Mechanical Systems and Signal Processing, **242**, pp. 1–10 (2026).
4. R.R. Kumar, L.O. Waisale, J.L. Tamata, A. Tortella, S.H. Kia, M. Andriollo, *Advanced fault detection and severity analysis of broken rotor bars in induction motors: Comparative classification and feature study using dimensionality reduction techniques*, Machines, **12**, *12*, pp. 1–10 (2024).
5. S.R. Mortezaei, M.H. Aliabadi, S. Javadi, *Eccentricity fault detection in surface-mounted permanent magnet synchronous motors by analytical prediction, FEM evaluation, and experimental magnetic sensing of the stray flux density*, Journal of Magnetism and Magnetic Materials, **589**, pp. 1–10 (2024).
6. N.A.R. Maciejewski, R.Z. Freire, A.L. Szejka, T.P.M. Bazzo, V.B. Frencl, A.E. Treml, *Comparative analysis of feature selection and classification techniques for robust broken rotor bar diagnosis in induction motors using current and vibration signals*, Auton. Intell. Syst., **5**, *1*, pp. 1–10 (2025).
7. M.B. Shahid et al., *Model predictive control for energy efficient AC motor drives: An overview*, IET Electric Power Appl., **18**, *12*, pp. 1894–1920 (2024).
8. R.P.P. de Souza, C.M. Agulhari, A. Goedtel, D. Moriñigo-Sotelo, Ó. Duque-Pérez, V. Fernández-Cavero, *Broken rotor bar fault detection – A virtual current approach combined with a robust linear parameter-varying observer*, Control Engineering Practice, **156**, pp. 1–10 (2025).
9. P. Pohakar, R. Gandhi, S. Hans, G. Sharma, P.N. Bokoro, *Analysis of multiple faults in induction motor using machine learning techniques*, e-Prime - Advances in Electrical Engineering, Electronics and Energy, **12**, pp. 1–10 (2025).
10. R.R. Kumar, L.O. Waisale, J.L. Tamata, A. Tortella, S.H. Kia, M. Andriollo, *Advanced fault detection and severity analysis of broken rotor bars in induction motors: Comparative classification and feature study using dimensionality reduction techniques*, Machines, **12**, *12*, pp. 1–10 (2024).
11. Y. Bendjeddou, A. Seghiour, M. Taib, H. Sellamna, A. Tertag, N. Benouzza, *Design sensitivity analysis and performance improvement of a six-phase squirrel-cage induction machine*, Rev. Roum. Sci. Techn. – Électrotechn. et Énerg., **71**, *1*, pp. 3–8 (2026).
12. A. Mabrek, Z. Elyazid, B. Selmoune, K.E. Hemsas, *Modeling broken rotor bar faults in induction motors: A combined SSFR and FEM approach*, Bulletin EEI, **14**, *6*, pp. 4356–4367 (2025).